

Interdecadal modulation of ENSO teleconnections to the Indian Ocean Basin Mode and their relationship under global warming in CMIP5 models

Weichen Tao,^{a,b} Gang Huang,^{c,d*} Kaiming Hu,^b Xia Qu,^b Guanhan Wen^b and Hainan Gong^b

^a LASG, Institute of Atmospheric Physics, Chinese Academy of Sciences, Beijing, and Chengdu University of Information Technology, China

^b Center for Monsoon System Research, Institute of Atmospheric Physics, Chinese Academy of Sciences, Beijing, China

^c Key Laboratory of Regional Climate-Environment for East Asia, Institute of Atmospheric Physics, Chinese Academy of Sciences, Beijing, China

^d Collaborative Innovation Center on Forecast and Evaluation of Meteorological Disasters, Nanjing, China

ABSTRACT: On the basis of Coupled Model Intercomparison Project phase 5 (CMIP5) models, this study have examined the ability of models to capture the El Niño/Southern Oscillation (ENSO)–Indian Ocean Basin Mode (IOBM) relationship, and investigated the characteristics of interdecadal change of ENSO–IOBM relationship as well as the response of the ENSO–IOBM relationship to the global warming. Among 23 CMIP5 models, the capability of models in representing the IOBM depends largely on the simulation of ENSO. Moreover, half of the models can reproduce the unstable ENSO–IOBM relationship. Considering the simulations of ENSO, ENSO–IOBM relationship and interdecadal change, 6 of 23 CMIP5 models are chosen for further investigation. The interdecadal change of ENSO–IOBM relationship is relative to the three ENSO-related processes. During the high correlation (HC) period, the tropospheric temperature (TT) mechanism, oceanic Rossby waves and antisymmetric wind pattern are strong, prolonging the persistence of IOBM. In comparison, during the low correlation (LC) period, the three processes are weak. The results show that the shallow thermocline in the southwestern Indian Ocean (SWIO), increased interannual variability and prolonged periodicity of ENSO are all responsible for the interdecadal change.

Furthermore, the possible changes of ENSO–IOBM relationship in the future are investigated. The ENSO-related tropical Indian Ocean (TIO) warming is strengthened under global warming. Despite the deepened thermocline over SWIO and unchanged ENSO activity, the ENSO-related TIO warming is strengthened by the enhanced TT mechanism, which is caused by the increased saturated specific humidity. The results reveal that there is more downward net heat flux (NHF) over the TIO, which is conducive to the TIO warming, and the latent heat flux (LHF) change makes a great contribution to the NHF change. The weakened upward or strengthened downward LHF is possibly due to the decreased anomalous sea–air temperature difference by strengthened TT mechanism.

KEY WORDS ENSO–IOBM relationship; Global warming; Future change; CMIP5; TT mechanism; sea–air temperature difference

Received 15 September 2013; Revised 13 February 2014; Accepted 25 February 2014

1. Introduction

The interannual sea surface temperature (SST) variation in the Indian Ocean exerts a great influence on the surrounding regions. The first leading mode of the interannual Indian Ocean SST variability features a basin-wide warming or cooling, called as IOBM (Indian Ocean Basin Mode; Yulaeva and Wallace, 1994; Klein *et al.*, 1999; Alexander *et al.*, 2002; Chowdary and Gnanaseelan, 2007; Du *et al.*, 2009; Schott *et al.*, 2009; Chakravorty *et al.*, 2013; Tao *et al.*, 2013). When IOBM is in the warming state, warm tropospheric Kelvin wave is triggered, which can contribute to the development of an anomalous anticyclone

over the Northwest Pacific (NWP) via the ‘capacitor effect’ (Xie *et al.*, 2009), the meridional displacement of the East Asian jet (EAJ) (Qu and Huang, 2012b) and the intensity of the South Asia high (SAH; Huang *et al.*, 2011; Qu and Huang, 2012a), and thus affect the East Asian climate, including summer rainfall (Xie *et al.*, 2010), typhoon (Du *et al.*, 2011), high temperature extremes (Hu *et al.*, 2011, 2012a, 2012b) and so on.

IOBM generally develops during the boreal winter when El Niño/Southern Oscillation (ENSO) matures, reaches its peak in the following spring (Alexander *et al.*, 2002; Lau and Nath, 2003; Schott *et al.*, 2009), and persists into the summer (Du *et al.*, 2009). Numerous studies have investigated the mechanisms for the formation of the basin-wide warming in the Indian Ocean. Lau and Nath (1996) showed that El Niño-induced anomalous atmospheric circulation can cause this warming through reducing surface evaporation and increasing incoming short wave radiation, which

* Correspondence to: G. Huang, Key Laboratory of Regional Climate-Environment for East Asia, Institute of Atmospheric Physics, Chinese Academy of Sciences, Beijing 100029, China. E-mail: hg@mail.iap.ac.cn

is known as ‘atmospheric bridge’ mechanism. The spread of tropospheric temperature (TT) anomalies associated with the propagation of El Niño-induced equatorial planetary waves from the eastern Pacific to the remote Tropics is an important process in such atmospheric bridge, which is also called TT mechanism (Chiang and Sobel, 2002; Chiang and Lintner, 2005). Klein *et al.* (1999) reported that net surface heat flux anomalies can explain most of the tropical Indian Ocean (TIO) warming, but the tropical southwestern Indian Ocean (SWIO) is an exception, suggesting that ocean dynamics is important there, which is further proved in model study (Lau and Nath, 2000). Murtugudde and Busalacchi (1999) and Yu and Rienecker (1999) also showed that ocean dynamics plays a significant role in the TIO SST warming. Masumoto and Meyers (1998) reported that there are anticyclonic wind anomalies over the south TIO during the developing and mature phases of El Niño, which cause the downwelling Rossby wave. The Rossby wave propagates to the SWIO where the thermocline is shallow and the Rossby wave is responsible for the SST rising there (Xie *et al.*, 2002). Chowdary *et al.* (2009) pointed out that barrier layer propagation and subsurface temperature upward propagation along thermocline are also important for SWIO warming. After the warming of SWIO, the SST anomalies increase the atmospheric convection there in the boreal spring following the El Niño (Xie *et al.*, 2002). The intensified convection excites an equatorially antisymmetric pattern of wind anomalies as a key to the IOBM persisting into boreal summer by reducing the prevailing southwest monsoon and so as to the latent heat flux (Du *et al.*, 2009). Above processes illustrate the importance of regional air–sea interaction and ocean dynamics in the Indian Ocean, not simply a passive response to ENSO.

However, the IOBM is not always strong and does not always persist through boreal summer (Du *et al.*, 2009; Huang *et al.*, 2010; Xie *et al.*, 2010). Both observational and atmospheric general circulation model (AGCM) studies show that the IOBM experienced an interdecadal change around the climate regime shift of the 1970s (Huang *et al.*, 2010; Xie *et al.*, 2010; Chowdary *et al.*, 2012). During the post-regime shift epoch, the ENSO-induced Rossby waves, the SWIO warming, the antisymmetric wind pattern, the North Indian Ocean (NIO) second warming are more pronounced than the pre-regime shift epoch. The magnitude and periodicity of ENSO increase around the 1970s (Wang *et al.*, 2008), and the thermocline shoals over the SWIO, which intensifies thermocline feedback, leading to this interdecadal change (Xie *et al.*, 2010; Chowdary *et al.*, 2012).

The air–sea interactions in the Indian Ocean and the interdecadal change of IOBM are important for the prediction of climate over the Indian Ocean and its surrounding regions. The World Climate Research Programme’s (WCRP’s) Coupled Model Intercomparison Project phase 3 (CMIP3) and phase 5 (CMIP5) provide good opportunities to explore the mechanisms for the air–sea interactions and interdecadal change as well as for future climate change with coupled ocean–atmosphere

general circulation models (CGCMs). Several studies have used these models to investigate the response of IOBM to ENSO. Saji *et al.* (2006) found 15 of 17 models in CMIP3 reproduce the IOBM a few months after ENSO. The models without IOBM usually have weak or bad ENSO simulations. A latest study that extended Saji *et al.* (2006) work using 20 models in CMIP5 reported that these models can reproduce the close relationship between ENSO and IOBM, and half of these models capture the key processes over the Indian Ocean (Du *et al.*, 2013). Their work is the first CMIP study examining the development of IOBM’s geographic patterns that are due to local ocean–atmosphere interactions. Furthermore, an ongoing study using CMIP5 models reveals that the impact of ENSO on NWP anticyclone is strengthened under the global warming scenario because of the response in TT anomalies. The strengthened relationship between ENSO and TIO SST anomalies is one of the reasons for the increase of TT anomalies (Hu *et al.*, 2013, personal communication).

Previous studies have investigated the relationship between ENSO and IOBM both in CMIP3 and CMIP5 simulations (Saji *et al.*, 2006; Chu *et al.*, 2013; Du *et al.*, 2013). Du *et al.* (2013) first revealed the interdecadal characteristics of IOBM using historical scenario simulations of CMIP5 models. On the basis of their work, the purpose of our study is to examine in depth the interdecadal characteristics of the ENSO–IOBM relationship and their relationship in future scenario. It finds that some of the models can capture the interdecadal change in the ENSO–IOBM relationship. The teleconnection and the internal coupled ocean–atmosphere dynamics related to the magnitude of ENSO, and the thermocline depth over the SWIO are all important for the interdecadal change in CMIP5 models, which are consistent with results based on observations (Xie *et al.*, 2010). Our results also show the possible reasons why the relationship between ENSO and IOBM is strengthened under global warming.

The rest of the article is organized as follows. Section 2 describes the CMIP5 models, data and methods. Section 3 investigates the relationship between ENSO and the Indian Ocean climate in historical run. Section 4 presents the characteristics for interdecadal change, including TT mechanism, ocean dynamics and antisymmetric wind pattern. Section 5 examines the changes in the relationship between ENSO and IOBM under global warming. Section 6 provides the summary.

2. Data and methods

This study is based on the CMIP5 output. We analyse two sets of simulations: the historical scenario simulations and the RCP45 scenario simulations. The historical experiments were conducted based on observed history of anthropogenic and natural forcing from 1870 to 2006. The RCP45 experiments were conducted from 2006 to 2100 driven by prescribed forcing (Thomson *et al.*, 2011), with the radiative forcing reaching about 4.5 Wm^{-2} near 2100. The detailed information is referred to the following web

Table 1. The CMIP5 models used in this study.

No.	Model name	Institute (Country)	AGCM resolution	OGCM resolution
1	BCC-CSM1.1	Beijing Climate Center (China)	128 × 64L17	360 × 232L40
2	CanESM2	Canadian Centre for Climate Modeling and Analysis (Canada)	128 × 64L22	256 × 192L40
3	CCSM4	National Center for Atmospheric Research (USA)	288 × 192L17	320 × 384L60
4	CNRM-CM5	Centre National de Recherches Meteorologiques (France)	256 × 128L17	362 × 292L42
5	CSIRO-Mk3.6.0	Atmospheric Research (Australia)	192 × 96L18	192 × 189L31
6	FGOALS-s2	LASG, Institute of Atmospheric Physics (China)	128 × 108L17	360 × 196L30
7	GFDL-CM3	NOAA Geophysical Fluid Dynamics Laboratory (USA)	144 × 90L23	360 × 200L50
8	GFDL-ESM2G	NOAA Geophysical Fluid Dynamics Laboratory (USA)	144 × 90L17	360 × 210L50
9	GFDL-ESM2M	NOAA Geophysical Fluid Dynamics Laboratory (USA)	144 × 90L17	360 × 200L50
10	GISS-E2-H	NASA Goddard Institute for Space Studies (USA)	144 × 89L17	144 × 90L33
11	GISS-E2-R	NASA Goddard Institute for Space Studies (USA)	144 × 89L17	288 × 180L32
12	HadCM3	Met Office Hadley Centre (UK)	96 × 73L17	288 × 144L20
13	HadGEM2-CC	Met Office Hadley Centre (UK)	192 × 144L17	360 × 216L40
14	HadGEM2-ES	Met Office Hadley Centre (UK)	192 × 144L23	360 × 216L40
15	INM-CM4	Institute for Numerical Mathematics (Russia)	180 × 120L17	360 × 340L40
16	IPSL-CM5A-LR	Institut Pierre-Simon Laplace (France)	96 × 96L17	182 × 149L31
17	IPSL-CM5A-MR	Institut Pierre-Simon Laplace (France)	144 × 143L17	182 × 149L31
18	MIROC5	Center for Climate System Research (The University of Tokyo) (Japan)	256 × 128L17	256 × 224L50
19	MIROC-ESM	Japan Agency for Marine-Earth Science and Technology (Japan)	128 × 64L35	256 × 192L44
20	MIROC-ESM-CHEM	Japan Agency for Marine-Earth Science and Technology (Japan)	128 × 64L35	256 × 192L44
21	MPI-ESM-LR	Max Planck Institute for Meteorology (Germany)	192 × 96L25	256 × 220L40
22	MRI-CGCM3	Meteorological Research Institute (Japan)	320 × 160L23	360 × 368L51
23	NorESM1-M	Norwegian Climate Centre (Norway)	144 × 96L17	320 × 384L70

site: <http://cmip-pcmdi.llnl.gov/cmip5/>. In this study, we use the outputs from 23 models. Table 1 lists the names, institutions, countries and resolutions of models. Monthly mean outputs are used, including SST, air temperature, sea surface height (SSH), 850 hPa wind, LHF, sensible heat flux (SHF), long wave radiation (LWR) and short wave radiation (SWR). Only one member ('r1i1p1') run of each model is analyzed. The observation data of SST used here are from the Hadley Centre Sea ICE and Sea Surface Temperature dataset (HadISST; Rayner *et al.*, 2003). It has a $1^\circ \times 1^\circ$ horizontal resolution and covers the period from January 1870 to the present.

This study focuses on the interdecadal changes of interannual variability. To extract interannual signals, we perform a 3-month running average to reduce intraseasonal variability and calculate a 9-year running average to remove decadal and longer variation in each simulation. Hereafter, any month in the developing years of ENSO are identified by suffix (0) whereas any month in the decaying years of ENSO are identified by suffix (1). The Niño3.4 index is defined as SST anomalies averaged over the central and eastern equatorial Pacific (5°S – 5°N , 170° – 120°W). The IOBM index is defined as SST anomalies averaged over the TIO (20°S – 20°N , 40° – 100°E). The range of NIO is defined as 0° – 20°N ,

40° – 100°E . The multi-model ensemble (MME) is calculated by averaging over the six best models with equivalent weight. Regression and correlation analysis are also used. The significance levels of the results are evaluated with the standard two-tailed Student's *t*-test.

3. The relationship between ENSO and the Indian Ocean SST in historical scenario simulations

ENSO is an internal mode of ocean–atmosphere interaction in the tropical Pacific. ENSO not only dominates in the tropical Pacific region, but also plays an important role in shaping the variability of the Indian Ocean SST. During the mature phase of ENSO, IOBM begins to develop (Klein *et al.*, 1999; Huang and Kinter, 2002; Krishnamurthy and Kirtman, 2003). The IOBM is generally considered as a response to ENSO remote forcing (Klein *et al.*, 1999; Venzke *et al.*, 2000; Alexander *et al.*, 2002; Lau and Nath, 2003). The good or bad simulation of IOBM depends largely on the simulation of the ENSO in CMIP3 models (Saji *et al.*, 2006) and CMIP5 models (Bellenger *et al.*, 2013; Du *et al.*, 2013). In full consideration of the previous works of Saji *et al.* (2006) and Du *et al.* (2013), the simulation of ENSO and ENSO–IOBM relationship are analyzed in this section in order to choose

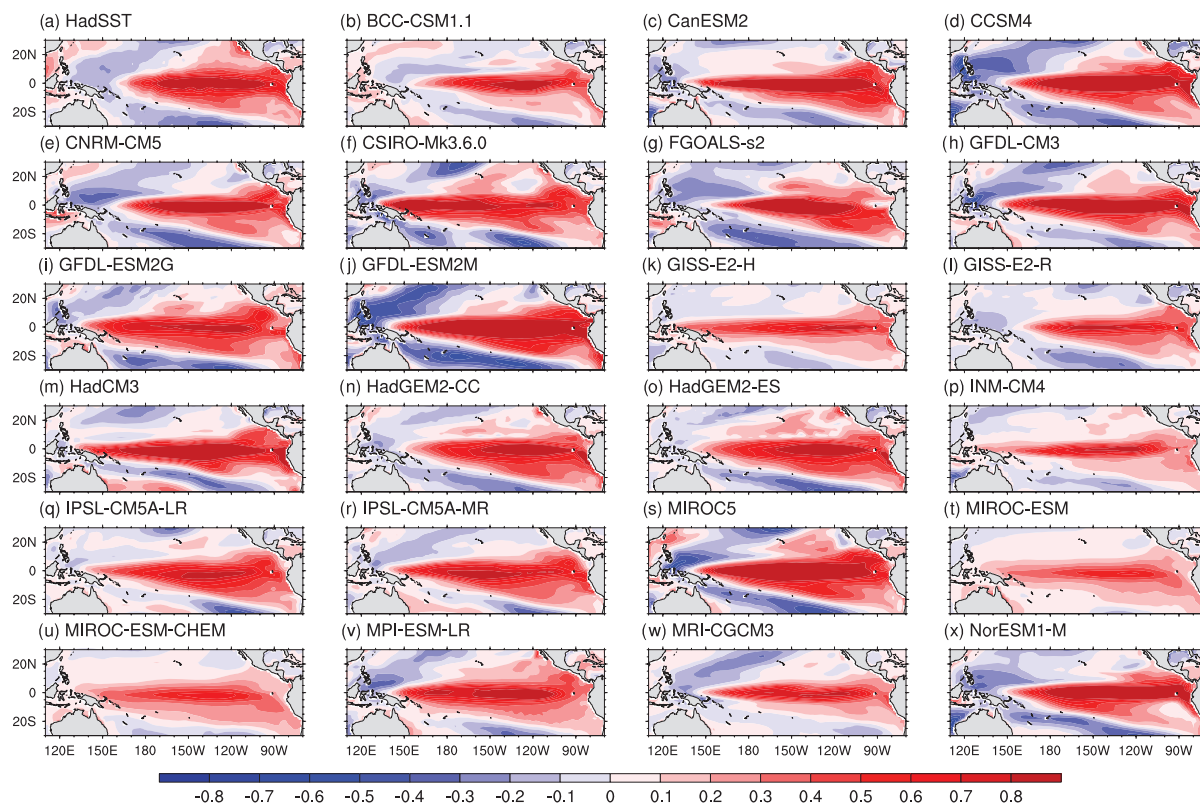


Figure 1. Regression of the DJF (0) tropical Pacific SST anomalies ($^{\circ}\text{C}$) with the simultaneous normalized Niño3.4 index in observation and 23 CMIP5 models for the period 1870–2004.

the proper models for us to further evaluate the projection in the future.

3.1. ENSO simulation and correlation with IOBM

Figure 1 presents the regression of the DJF (0) tropical Pacific SST anomalies with the simultaneous normalized Niño3.4 index. In observations, there are large positive anomalies over the tropical central and eastern Pacific (Figure 1(a)). In CMIP5 model simulations, the SST anomaly patterns vary in amplitude, location and areal extent (Figure 1(b)–(x)). Especially, in four models, including GISS-E2-H, INM-CM4, MIROC-ESM, MIROC-ESM-CHEM, the ENSO-related SST anomalies are weaker and extend too far west, even to the tropical western Pacific. Du *et al.* (2013) and Gong *et al.* (2013) also mentioned the departure of ENSO simulation in the Pacific. In addition, it is noted that the CSIRO-Mk3.6.0 model does not reproduce reasonable SST anomalies related to ENSO, with the maximum SST anomalies being located in the tropical western Pacific (Figure 1(f)). This bias is also mentioned by Kim and Yu (2012) and Gong *et al.* (2013).

In order to examine the response of IOBM to ENSO more clearly, it is reasonable to evaluate their relationship in models using scatter diagram. Figure 2 shows the relationship between the simulations of DJF (0) ENSO and MAM (1) IOBM. Generally, the poor SST spatial patterns compared with the observation weaken the ENSO–IOBM

relationship in CMIP5 models (Figure 2(a)). The correlation coefficient of ENSO–IOBM relationship and ENSO spatial correlation is 0.52 (containing observation), and its significant level reaches 99%. It implies that the capability of models in simulating the ENSO-related SST patterns influences the ENSO–IOBM relationship in CMIP5 models. Simultaneously, decreased interannual variability of ENSO corresponds to the weakened ENSO–IOBM relationship, and there exists a positive correlation between them in CMIP5 models (Figure 2(b)). The correlation coefficient of ENSO–IOBM relationship and ENSO variance is 0.66 (containing observation), exceeding the 99% significant level. Du *et al.* (2013) also drew the similar conclusion, though they used the JJA (1) IOBM index rather than MAM (1). Above all, the capability of models in representing the IOBM depends largely on the simulation of ENSO in CMIP5 models, which appears to be consistent with Saji *et al.* (2006) who used the CMIP3 models.

3.2. The unstable relationship between ENSO and IOBM

The ENSO–IOBM relationship shows an interdecadal change around the climate regime shift of the 1970s in observations and previous AGCM studies (Huang *et al.*, 2010; Xie *et al.*, 2010; Chowdary *et al.*, 2012). These mean that the ENSO–IOBM relationship is not always strong and mainly reflects in the persistence of TIO SST anomalies. Du *et al.* (2013) have discussed ENSO–IOBM relationship displays interdecadal variation in CMIP5

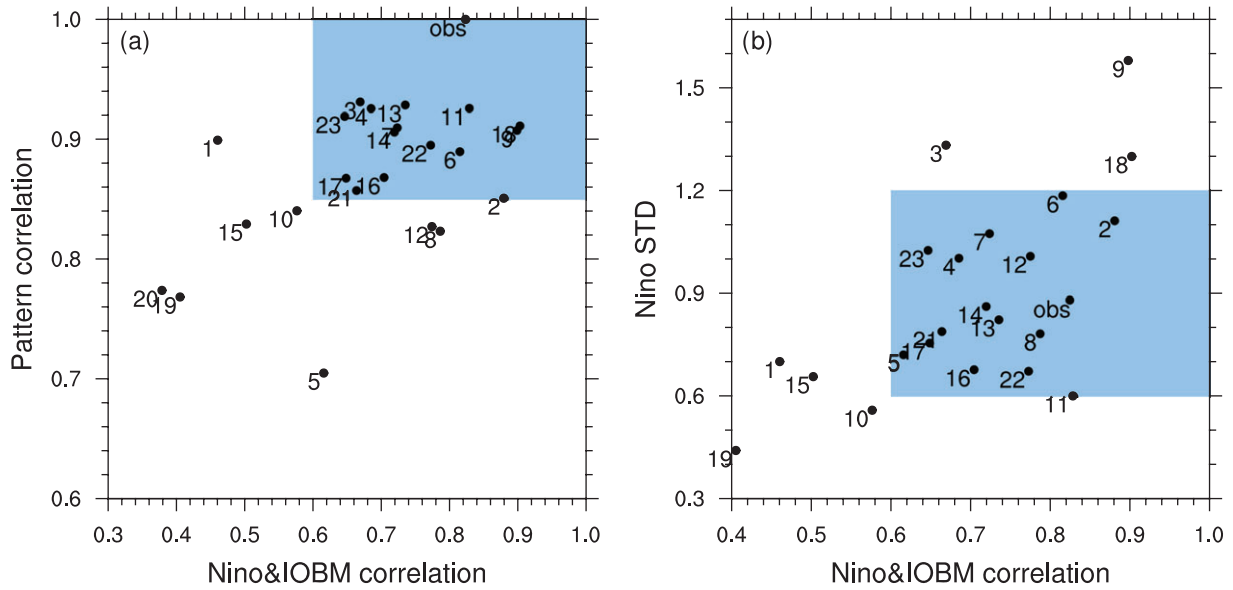


Figure 2. Relationship of ENSO and IOBM: (a) scatter diagram of pattern correlation coefficients of ENSO patterns, and correlation coefficients of the DJF (0) Niño3.4 index and MAM (1) IOBM index in observation and 23 CMIP5 models; (b) scatter diagram of standard deviations of DJF (0) Niño3.4 index, and correlation coefficients of the DJF (0) Niño3.4 index and MAM (1) IOBM index in observation and 23 CMIP5 models. Numbers represent the model numbers listed in Table 1. Blue shading indicates the limits defined by the first and second rules in Section 4.

models, and IOBM variance responds to ENSO amplitude modulations in the Pacific. Whether the CMIP5 models can capture the significant unstable relationship between ENSO and IOBM as the observation? Figure 3 presents the 25-year sliding correlation of DJF (0) Niño3.4 index and JJA (1) NIO index in 23 CMIP5 models and observations during 1870–2004. In observations, the sliding correlation coefficient has a sudden drop around the mid-1970s, consistent with previous study (Huang *et al.*, 2010). Most of the CMIP5 models can reproduce the significant unstable ENSO–IOBM relationship during 1870–2004. In 9 of 23 models, including CanESM2, CCSM4, FGOALS-s2, GFDL-CM3, GFDL-ESM2G, GFDL-ESM2M, HadCM3, MIROC5, NorESM1-M, the sliding correlation coefficients are stable during the analysis time period, which is consistent with CFSv1 results (Chowdary *et al.*, 2014; Figures 2(b) and 5(b)). In the rest of models, the sliding correlation coefficients feature interdecadal variations. Though the BCC-CSM1.1 model can capture multi-decadal oscillation, the sliding correlation coefficients are lower and even negative compared with the observations.

4. Characteristics of interdecadal change in historical scenario simulations

To study the characteristics of interdecadal change in CMIP5 models, it is reasonable to choose the proper models for further investigation. Simultaneously considering the simulation of ENSO, IOBM, their relationship and interdecadal change, there are three rules together for choosing models. First one is that the pattern correlation coefficients of ENSO-related SST anomalies are above 0.85 and the correlation coefficients between ENSO and

IOBM are above 0.6 (Figure 2(a); blue shading); Second one is that interannual variability of ENSO is from 0.6 to 1.2 and the correlation coefficients between ENSO and IOBM are above 0.6 (Figure 2(b); blue shading); Third one is that the differences between maximum and minimum of sliding correlation coefficients are above 0.35, which is listed in Table 2. The first and second rules artificially choose the models have a degree of fidelity at simulating the spatial pattern, interannual variability of ENSO and interannual ENSO–IOBM relationship. The third rule takes the interdecadal modulation of ENSO–IOBM relationship into consideration. Then 8 of 23 models are retained. Though IPSL-CM5A-LR and IPSL-CM5A-MR conform to the above three rules, their IOBM patterns have weak even cold SST anomalies over the southeastern Indian Ocean and South China Sea inconsistent with the observation (figure not shown). In addition, these two models cannot reproduce both the ocean dynamics and anti-symmetric wind pattern over the Indian Ocean (Du *et al.*, 2013; Figures 8, 11, and 13). Whether or not including these two models lead to similar results. So, we selected six best models: CNRM-CM5, GISS-E2-R, HadGEM2-CC, HadGEM2-ES, MPI-ESM-LR and MRI-CGCM3.

ENSO has three different teleconnection processes to influence the IOBM. One is ‘atmospheric bridge’ mechanism (Lau and Nath, 1996; Lau, 1997; Klein *et al.*, 1999), and TT mechanism is very important in such atmospheric bridge (Chiang and Sobel, 2002; Chiang and Lintner, 2005). The second process is the Rossby wave excited by ENSO-induced wind stress (Xie *et al.*, 2002), which prolongs the influence of ENSO on the IOBM after the mature phase of El Niño. The third process is the equatorially antisymmetry pattern of wind anomalies. It is a key process persisting the IOBM into boreal summer

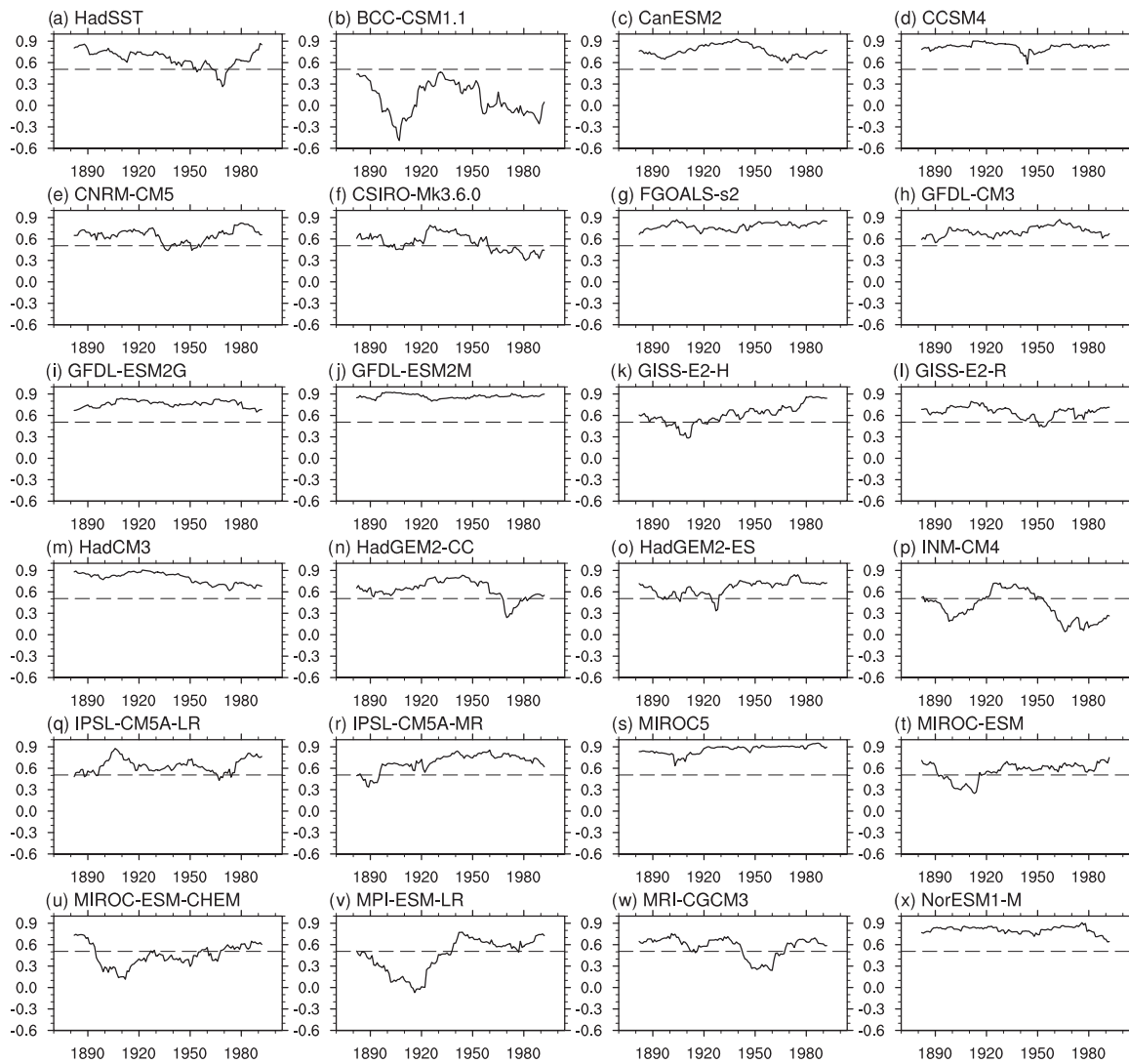


Figure 3. The 25-year sliding correlation of DJF (0) Niño3.4 index and JJA (1) NIO index in observation and 23 CMIP5 models for the period 1870–2004. The dashed lines indicate significant levels reach 95%.

(Du *et al.*, 2009). In observation, there is an interdecadal change in the TIO response to ENSO in the 1970s (Xie *et al.*, 2010; Chowdary *et al.*, 2012). Accordingly, the oceanic Rossby wave and the antisymmetric wind pattern are more pronounced during the post-regime shift (after 1970s) epoch than the pre-regime shift epoch. Strengthened ENSO and shallow thermocline are the two main factors for the interdecadal change (Xie *et al.*, 2010). Therefore, one question arises, whether the 6 models can reproduce realistic decadal change of above ENSO-related processes over the TIO? To answer this question, we examine the three processes using MME of six best models during the HC and LC periods, denoting the period with the highest and lowest correlation coefficient, respectively. The HC and LC periods are selected based on the 25-year sliding correlation of DJF (0) Niño3.4 index and JJA (1) NIO index (Figure 3). For convenience, we consider the climate anomalies in the decaying phase of El Niño, and the results are applicable to La Niña cases.

Table 2. The difference of maximum and minimum 25-year sliding correlation coefficient in observation and each model.

Names	Maximum – minimum	Names	Maximum – minimum
BCC-CSM1.1	0.96	HadGEM2-CC	0.59
CanESM2	0.33	HadGEM2-ES	0.51
CCSM4	0.33	INM-CM4	0.68
CNRM-CM5	0.39	IPSL-CM5A-LR	0.45
CSIRO-Mk3.6.0	0.49	IPSL-CM5A-MR	0.52
FGOALS-s2	0.21	MIROC5	0.32
GFDL-CM3	0.33	MIROC-ESM	0.50
GFDL-ESM2G	0.19	MIROC-ESM-CHEM	0.63
GFDL-ESM2M	0.13	MPI-ESM-LR	0.85
GISS-E2-H	0.58	MRI-CGCM3	0.52
GISS-E2-R	0.35	NorESM1-M	0.27
HadCM3	0.29	OBS	0.61

4.1. TT mechanism

ENSO is the dominant mode of air–sea interaction in the equatorial Pacific, and the connection between ENSO and

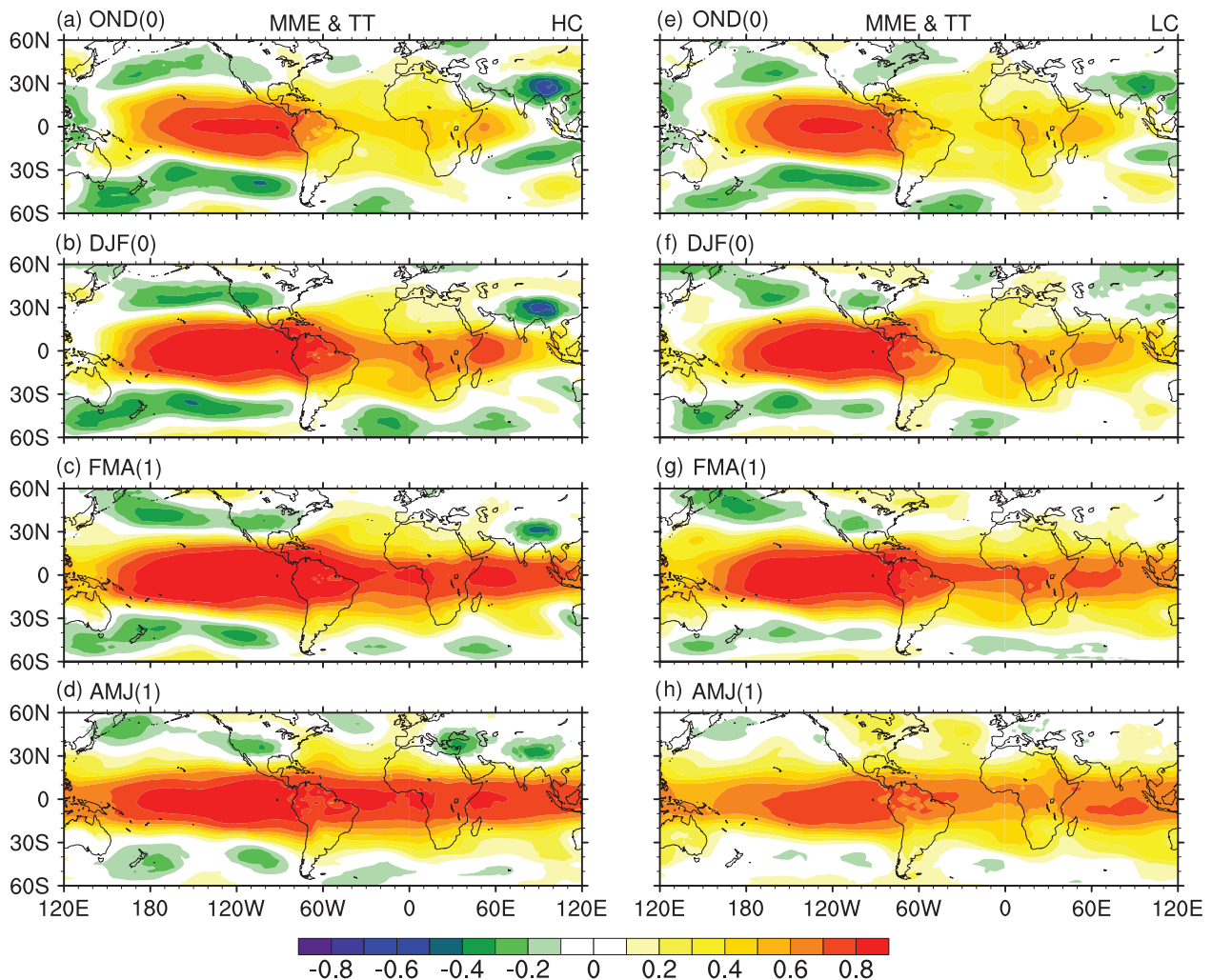


Figure 4. Multi-model ensemble correlation of 1000–200 hPa mean tropospheric temperature (TT) with DJF (0) Niño3.4 index during the period for HC (left panels, (a)–(e)), and the same during the period for LC (right panels, (f)–(j)). The left strings above each panel indicate the months lead or lag DJF (0): OND (0) implies TT leads Niño3.4 index 2 months, DJF (0) implies TT and Niño3.4 index are simultaneous, FMA (1) implies TT lags Niño3.4 index 2 months, AMJ (1) implies TT lags Niño3.4 index 4 months.

TT is well established (Horel and Wallace, 1981; Pan and Oort, 1983; Yulaeva and Wallace, 1994; Soden, 2000). TT over the tropical eastern Pacific warms with the SST increase, and there is the warming of entire tropical TT in the following months (Charney, 1963; Wallace, 1992; Sobel and Bretherton, 2000). During the developing phase of ENSO, significant TT anomalies illustrating the ‘dumb-bell shape’ characteristic occurs in the eastern and central Pacific. Su *et al.* (2003) said that atmospheric wave is the most effective way to spread the warm anomalies in free atmosphere. Therefore, after the establishment of the dumbbell shape, the transient Kelvin wave is consistent with the eastward of TT anomalies. Chiang and Sobel (2002) reported ENSO influences the remote region by the propagation of TT and that the remote ENSO impact is the adjustment of the remote tropical climate to the TT perturbation, which is defined as the TT mechanism. In a subsequent study, Chiang and Lintner (2005) interpreted the TT mechanism in more detail, the equatorial wave communicates the TT anomalies to the remote region, increasing

the moist static energy of the free troposphere. Convective linkages compel the boundary layer moist static energy to vary with the free troposphere value, thus in turn, evaporation is reduced because of the increased boundary layer specific humidity. So the remote tropical ocean adjusts to the TT forcing, and warms up eventually. In such mechanism, LHF is the important regulator linking the surface warming to the tropospheric warming.

Chiang and Sobel (2002) indicated that the TT mechanism is more or less the Walker circulation mechanism, just posed in a different way of the ‘atmospheric bridge’ mechanism. The lead–lag correlation of 1000–200 hPa mean TT with DJF (0) Niño3.4 index during the period for HC and LC in MME are presented in Figure 4. The ENSO-related persistent warming in the east Pacific, through convection and moist adjustment, heats the whole tropospheric column there, and forms the Matsuno–Gill pattern (Matsuno, 1966; Gill, 1980) in TT. As time goes on, the warm pattern develops and extends to the east by forcing the Kelvin wave eastward and affects the climate

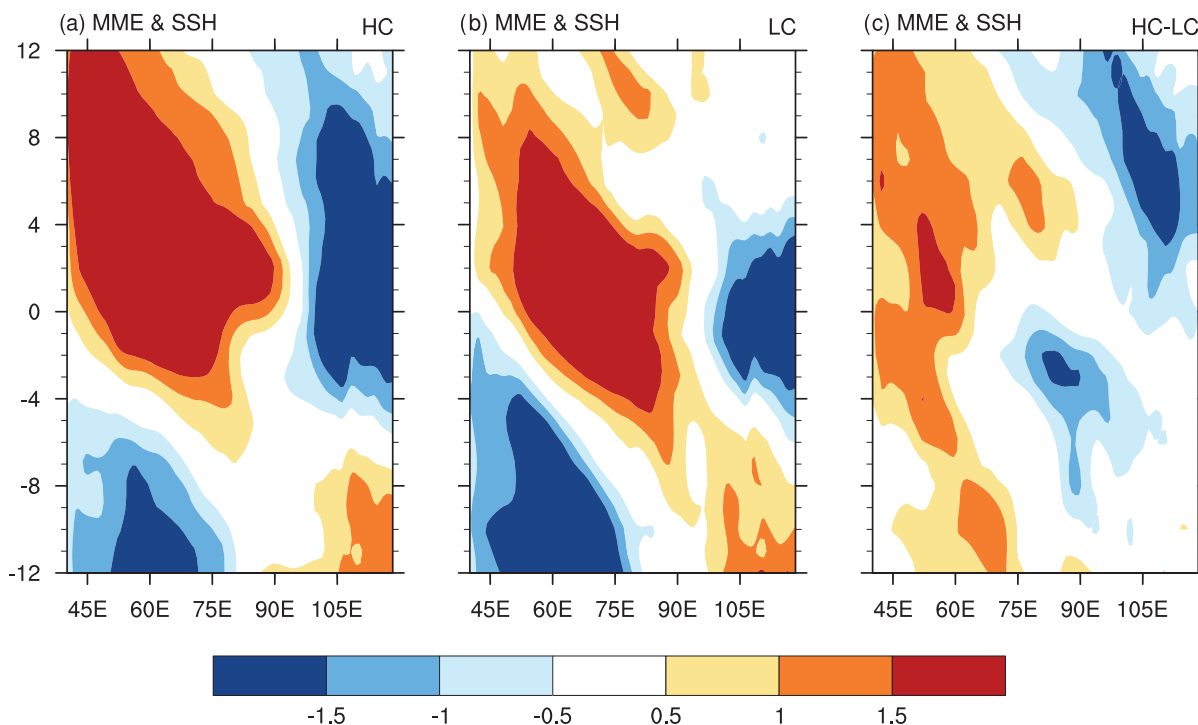


Figure 5. Multi-model ensemble regression of SSH (cm), averaged in 8°S – 12°S , with DJF (0) Niño3.4 index for (a) the HC period, (b) LC period and (c) HC minus LC differences as a function of longitude and calendar month.

of the Indian Ocean. When TT lags DJF (0) Niño3.4 index 2 and 4 months, the ENSO-related TT anomalies over the TIO are more pronounced in the HC period than LC period. The result shows that TT mechanism is relatively strong in the HC period.

4.2. Oceanic Rossby wave

According to the TT mechanism, the tropical Indian Ocean warming is attributed to the influence of atmosphere. In some regions, however, oceanic processes play a more important role in the development of TIO SST anomalies. Xie *et al.* (2002) posed that a westward-propagating downwelling Rossby wave in the SWIO forced by the anomalous easterlies in the equatorial Indian Ocean, induces positive SST anomalies there.

Figure 5 presents the lead-lag regression of SSH (averaged in 8°S – 12°S) with DJF (0) Niño3.4 index for the HC period, LC period and HC minus LC differences in MME as a function of longitude and calendar month. The maximum SSH anomalies begin to appear at 90°E in June and reach about 60°E in May of the following year. The thermocline deepens in the southeast TIO in response to the anomalous anticyclone there first (Masumoto and Meyers, 1998). Then the pronounced oceanic Rossby wave propagates westward slowly to the SWIO (Figure 5(a) and (b)) where the mean thermocline is shallow. The Rossby wave deepens thermocline, and raises SST there (Xie *et al.*, 2002; Chowdary *et al.*, 2009). In comparison, the SSH anomalies are stronger and sustained longer during the HC period than during the LC period, indicating the oceanic Rossby wave is stronger and the duration is longer

(Figure 5(c)). This characteristic is consistent with the interdecadal change in observations. Compared with the post-regime shift epoch, the westward-propagating Rossby wave is much weaker for the pre-regime shift epoch (Xie *et al.* 2010; Figure 9).

4.3. Antisymmetric wind pattern

After the warming of SWIO, the cross-equatorial SST gradient excites an equatorially antisymmetric wind pattern as a key to the IOBM persisting into boreal summer by reducing the prevailing southwesterly monsoon during boreal spring, and so as the LHF as a result of wind-evaporation-SST (WES) feedback (Xie and Philander, 1994; Wu *et al.*, 2008; Du *et al.*, 2009; Wu and Yeh, 2010).

Figure 6 compares the evolution of ENSO-related SST and 850 hPa wind anomalies from DJF (0) to JJA (1) for the HC period, LC period and HC minus LC differences. When an El Niño event takes place, there are basin-wide warming in the TIO and anomalous easterlies over the equatorial Indian Ocean during DJF (0) in both periods (Figure 6(a) and (d)). During MAM (1), warm SST anomalies still maintain over the TIO, but the SST anomalies in the SWIO are stronger than in the NIO, forming a cross-equatorial SST gradient. Consistent with such SST pattern, 850 hPa wind anomalies feature an antisymmetric pattern, with northeasterlies north and northwesterlies south of the equator (Figure 6(b)). The anomalous northwesterlies strengthen SST warming in the SWIO by reducing the southeasterly trade winds, while the northeasterlies weaken SST warming in the NIO before May

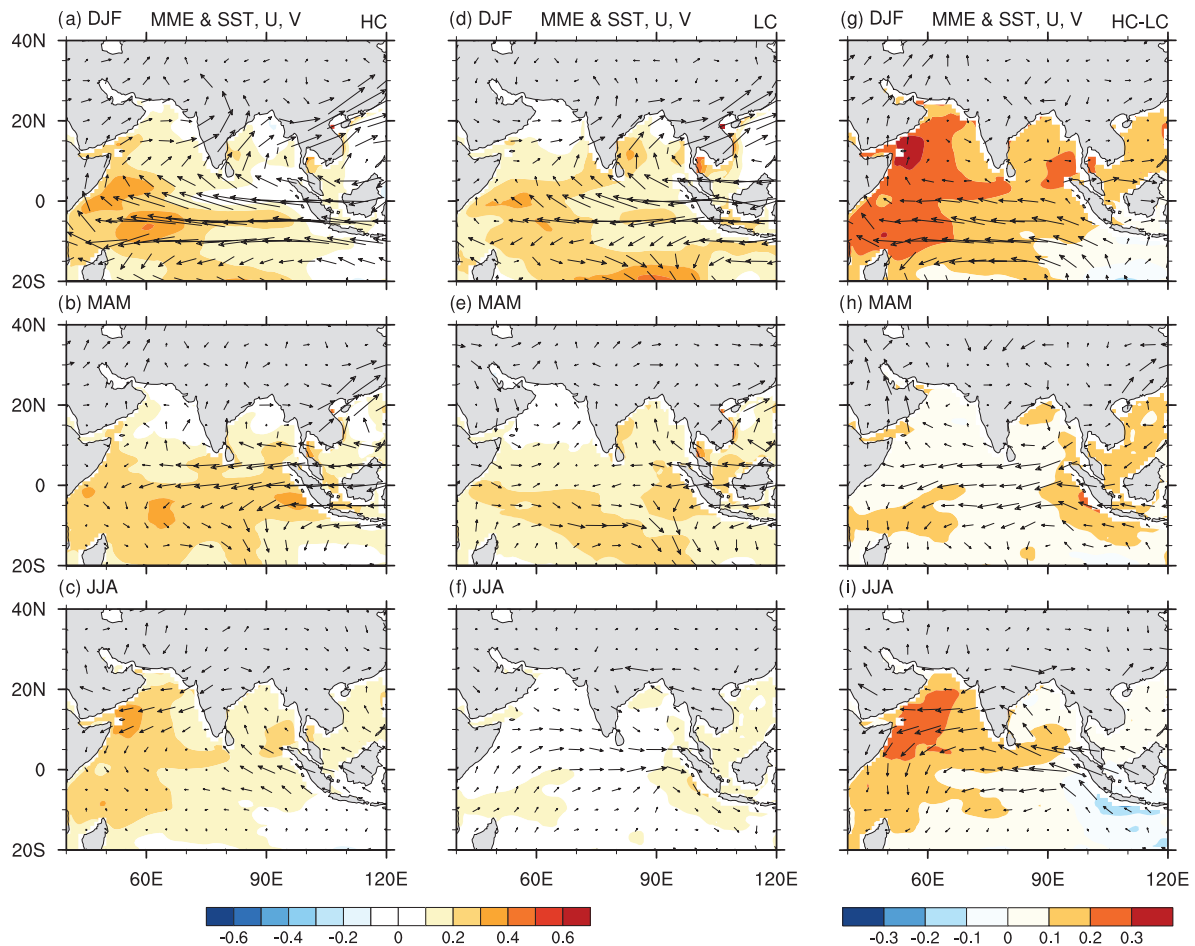


Figure 6. Multi-model ensemble regression of SST ($^{\circ}\text{C}$) and 850 hPa wind velocity (m s^{-1}) with DJF (0) Niño3.4 index during DJF (0), MAM (1) and JJA (1) for the HC period (left panels, (a)–(c)), LC period (middle panels, (d)–(f)) and HC minus LC differences (right panels, (g)–(i)).

by strengthening the mean northeasterly monsoon (Kawamura *et al.*, 2001; Wu *et al.*, 2008; Park *et al.*, 2010) and strengthen SST warming after the southwest monsoon onset in May (Du *et al.*, 2009). The interaction between SST gradient and wind pattern is a positive feedback mechanism called WES feedback (Xie and Philander, 1994). Through the cross-equatorial SST gradient is still obvious, the antisymmetric wind anomalies are weak for the LC period (Figure 6(e)). There seems a little disagreement between the disappearance of antisymmetric wind anomalies and cross-equatorial SST gradient in the LC period, but the wind anomalies are weakened. As the result of antisymmetric wind pattern and shift in monsoon, the IOBM sustains through JJA (1) (Figure 6(c)). While in the LC period, there are no obvious SST anomalies in the TIO (Figure 6(f)). In observations, the post-regime shift epoch is also characterized by an antisymmetric wind pattern but not the pre-regime shift epoch (Xie *et al.*, 2010). The second warming of NIO leads to the enhancement of the TIO capacitor, which influences the NWP anticyclone in both observations (Xie *et al.*, 2010) and CMIP5 models (Hu *et al.*, 2013, personal communication).

Why the IOBM can persist through JJA (1) in the HC period? Previous study has examined the possible reasons

for it. Xie *et al.* (2010) reported that the magnitude and periodicity of ENSO increases around the 1970s, and the thermocline shoals over the SWIO, leading to the interdecadal change in observation. Chowdary *et al.* (2012) also demonstrated the role of ENSO using ship observation from 1870 to 2007. Figure 7(a) shows the difference of climatology SSH during MAM (1) between the HC and LC period for MME. There are negative climatology SSH anomalies over the SWIO, indicating that the climatological thermocline shoals there in the HC period. The shallower thermocline causes a stronger thermocline feedback. Intensified thermocline feedback (Figure 7(a)) and strengthened ocean processes (Figure 5(a)) both contribute to the persistence of SWIO warming in the HC period. The strengthened ocean processes, the enhanced antisymmetric wind pattern and the second warming of NIO are associated with increased interannual variability and prolonged periodicity of ENSO (Xie *et al.*, 2010). Figure 7(b) and (c) shows the standard deviation of DJF (0) Niño3.4 index between the two periods for six best CMIP5 models and the autocorrelation of Niño3.4 index with its DJF (0) values for MME, respectively. The standard deviation of ENSO is larger during the HC period than during the LC period in every model (Figure 7(b)). Du *et al.* (2013) also revealed

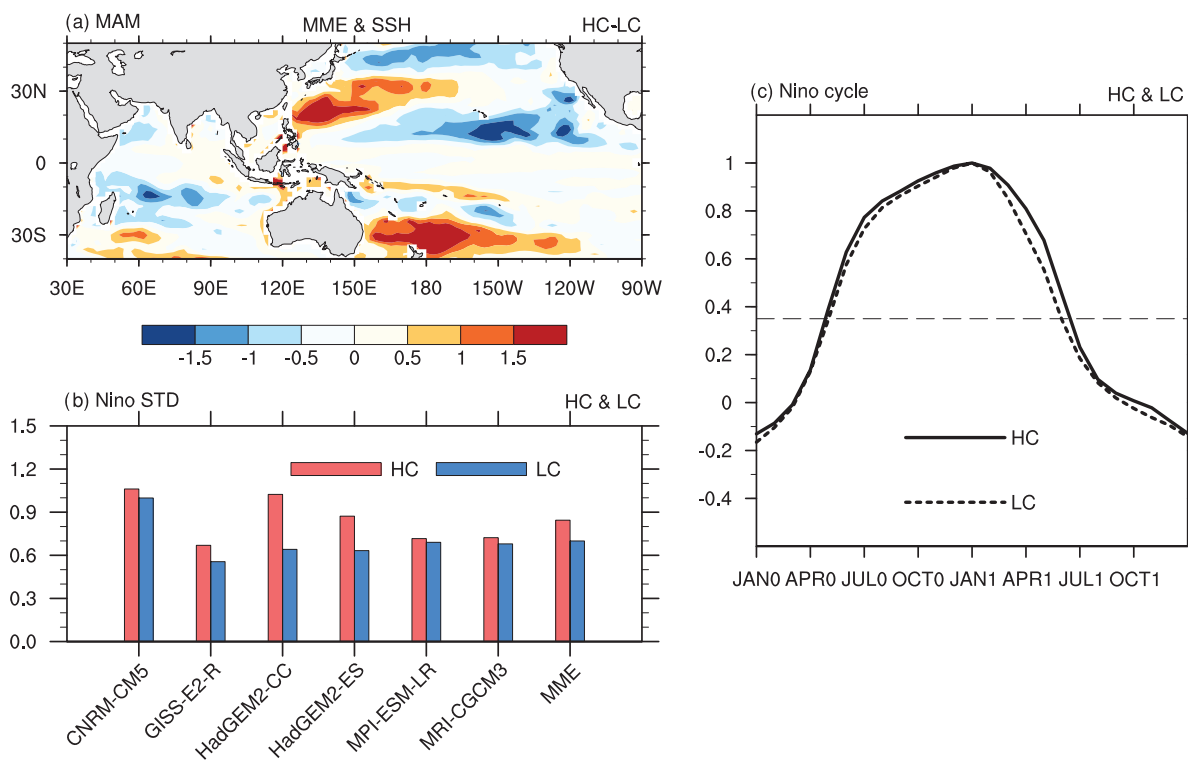


Figure 7. (a) Multi-model ensemble difference of climatology SSH (cm) during MAM (1) between the HC and LC period. (b) Standard deviation of DJF (0) Niño3.4 index in the HC and LC period for six best CMIP5 models and MME. (c) Multi-model ensemble autocorrelation of Niño3.4 index with its DJF (0) values in the HC and LC period.

that the ENSO–IOBM correlation coefficient is low when ENSO variance is low in almost all CMIP5 models, first suggesting the ENSO variances control the ENSO–IOBM relationship. In Figure 7(c), the decay of ENSO is about 1 month later in the HC period than in the LC period. Above all, shallower thermocline, increased interannual variability and prolonged periodicity of ENSO during the HC period are all responsible for the interdecadal change in CMIP5 models. This is also consistent with an ongoing article of Hu *et al.* (2013, personal communication), which pay more attention on the relationship between ENSO and NWP climate via the Indian Ocean capacitor effect during boreal summer in CMIP5 models.

5. IOBM in RCP45 scenario simulations

A better understanding of the relationship between ENSO and IOBM is important for the prediction of the Indian Ocean SST anomalies and associated climate anomalies. Above sections demonstrate that the six best models can capture the interdecadal change between ENSO and IOBM. On the basis of the historical and RCP45 scenario simulations, these models are useful to investigate the possible changes and underlying mechanism of ENSO-related TIO warming in the future.

Figure 8 shows the 25-year sliding regression of TIO and NIO SST with the DJF (0) Niño3.4 index as a function of calendar month and year. Over the entire TIO, the positive SST anomalies peak at boreal spring after the mature phase

of ENSO (Figure 8(a)). The ENSO-related SST anomalies are strengthened since 1940s until the late 21st century. During the late 20th century and middle 21st century, there are significant SST anomalies in the TIO. Consistent with TIO, the SST anomalies in the NIO is also strengthened since 1940s. However, there seems to be a linear warming trend, as the SST anomalies are strengthened in late 20th century and further enhanced in the late 21st century (Figure 8(b)). Above illustrate that, though the NIO is part of TIO, the time and magnitude when ENSO-related SST anomalies are strengthened do not remain consistent in the TIO and NIO. It seems that different factors cause the enhanced SST anomalies in the 20th and 21st centuries over the TIO.

To further investigate the possible change of ENSO–IOBM relationship between the current and future climate as well as its underlying mechanism, we select three periods as follows to represent different background: 1870–1919 under historical scenario, 1950–1999 under historical scenario and 2049–2098 under RCP45 scenario. The periods of 1870–1919 and 1950–1999 under historical scenario represent the past and present climate background, respectively. The period of 2049–2098 under RCP45 scenario represents the future climate background. The correlation of monthly IOBM index with DJF (0) Niño3.4 index in the three periods for MME are shown in Figure 9. The IOBM develops in boreal fall, peaks in spring and persists into summer during 1870–1919. However, during 1950–1999 and

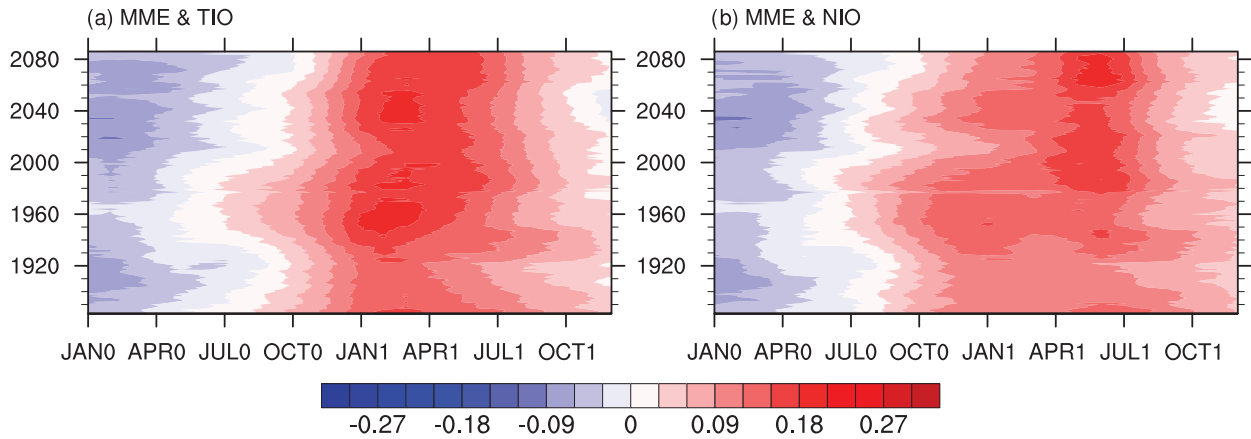


Figure 8. The 25-year sliding regression on DJF (0) Niño3.4 index as a function of calendar month and year for the developing and decaying years of ENSO: (a) SST (°C) over the TIO; (b) SST (°C) over the NIO.

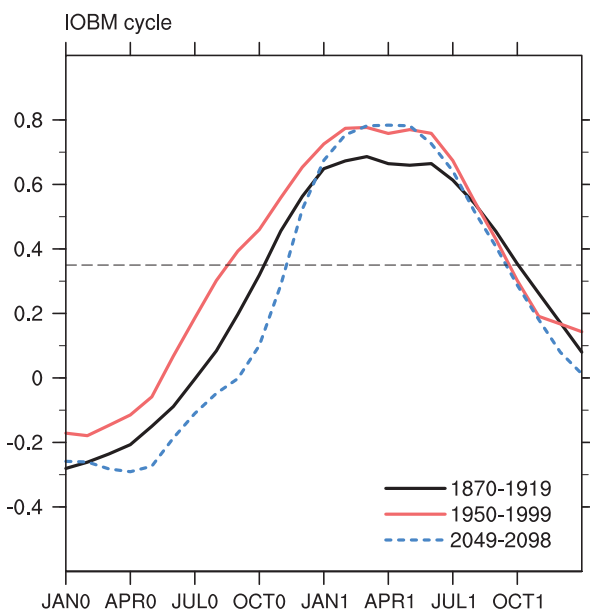


Figure 9. Multi-model ensemble correlation of monthly IOBM index with DJF (0) Niño3.4 index for the periods of 1870–1919 (black solid line), 1950–1999 (red solid line) and 2049–2098 (blue dashed line). The horizontal dashed line indicates significant level reaches 95%.

2049–2098, the correlation coefficients are about 0.1 larger than 1870–1919 from November (0) to July (1). Hu *et al.* (2013, personal communication) obtained a similar conclusion and reported that the correlation coefficients over the TIO during MJJ (1) are 0.1 higher both in the present and future periods. The results are also consistent with previous regression analysis (Figure 8(a)). Therefore, there are two questions arise: why the ENSO–IOBM relationship is strengthened and what role the increased anthropogenic gas concentrations may play in it?

5.1. Changes of SWIO thermocline and ENSO

To understand plausible reasons for the change in the above correlation, it is reasonable to examine the depth of thermocline and magnitude, periodicity of ENSO, which are demonstrated to be important by both observations and

models (Xie *et al.*, 2010; Hu *et al.*, 2013, personal communication). Figure 10 presents the changes of climatology SSH in the present and future relative to the past and inter-annual variability, periodicity of ENSO during the three periods. To eliminate the thermal effects, and retain the dynamic effects caused by the wind stress change, the tropical mean (30°S–30°N) value has been subtracted from the SSH change (Hu *et al.* 2013, personal communication). Figure 10(a) is similar to Figure 7(a), and the change of SSH between the present and past is negative in the SWIO, indicating the climatological thermocline shoals there in the present. Moreover, positive SSH anomalies are over the western Indian Ocean (WIO; Figure 10(b)), indicating that the climatological thermocline deepens there in the future. The rising SSH in the WIO is caused by the anomalous easterlies over the TIO, which is consistent with the influence of weakening Walker circulation under global warming (Held and Soden, 2006; Vecchi *et al.*, 2006; Tokinaga *et al.*, 2012; Zheng *et al.*, 2013). Previous studies showed the shallower thermocline is conducive to the thermocline feedback over the SWIO (Xie *et al.*, 2010), and vice versa. In Figure 10(c), the interannual variability of ENSO during the three periods varies among different models. For MME, the standard deviation of ENSO does not change much. It suggests that the interannual variability of ENSO does not experience significant change in the present and future. Collins *et al.* (2010) also reported that the ENSO amplitude is highly variable among models, and it is not yet possible to estimate the changes of ENSO. Furthermore, the evolution of ENSO in the present is consistent with the past, and slightly shorter in the future (Figure 10(d)). Considering these small changes, including the interannual variability and periodicity, ENSO activity is almost unchanged in the present and future. Accordingly, ENSO-related oceanic Rossby wave and antisymmetric wind pattern do not change much in the present and future (figure not shown). As mentioned before, the enhanced ENSO–IOBM relationship in the present is unlikely related to ENSO activity,

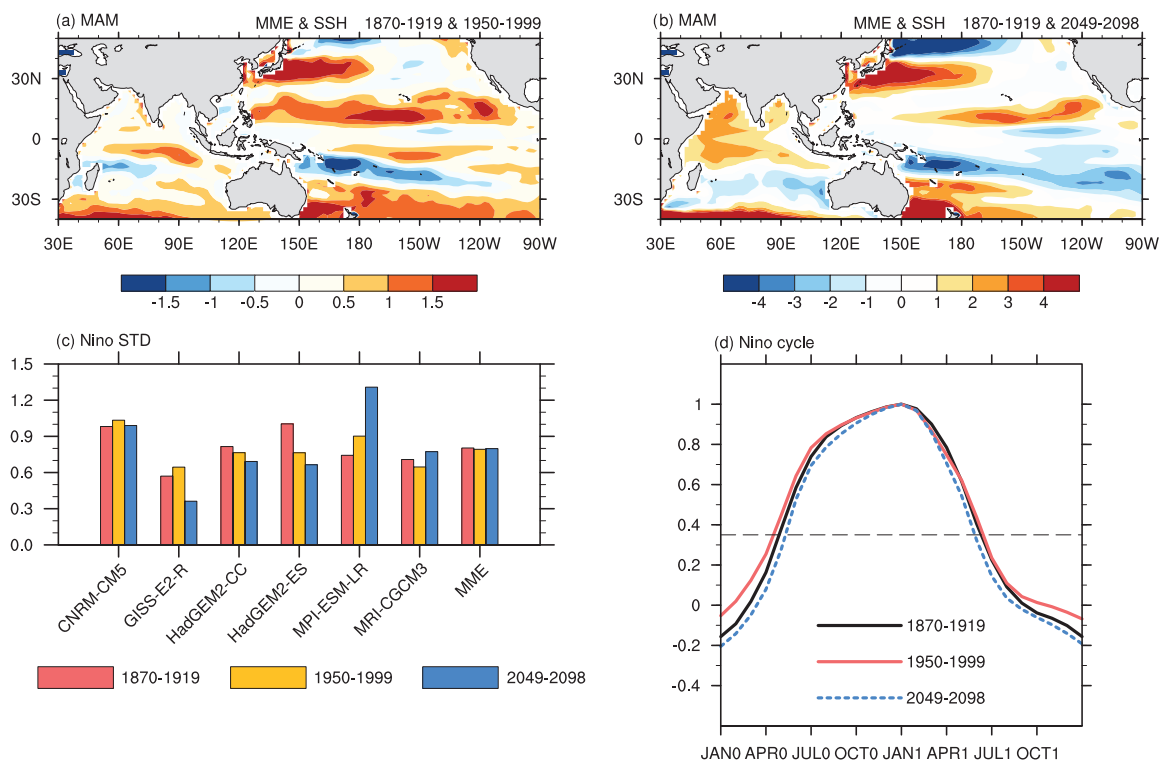


Figure 10. (a) Multi-model ensemble difference of climatology SSH (cm) during MAM (1) between the periods of 1870–1919 and 1950–1999. (b) Multi-model ensemble difference of climatology SSH (cm) during MAM (1) between the periods of 1870–1919 and 2049–2098. (c) Standard deviation of DJF (0) Niño3.4 index in the periods of 1870–1919, 1950–1999 and 2049–2098 for six best CMIP5 models and MME. (d) Multi-model ensemble autocorrelation of Niño3.4 index with its DJF (0) values in the periods of 1870–1919, 1950–1999 and 2049–2098.

and seems to be more related to the shallower climatological thermocline over the SWIO, which will be discussed in detail in Section 5.3. However, even the climatological thermocline deepens in the SWIO, why the ENSO–IOBM relationship is still strengthened in the future?

5.2. Possible reasons for the strengthened ENSO–IOBM relationship in the future

5.2.1. Enhanced TT mechanism

Despite the deepened thermocline and unchanged ENSO activity, both the SST anomalies over the TIO (Figure 8) and the correlation coefficients between ENSO and IOBM (Figure 9) are strengthened in global warming. Excluding the influence of ocean processes and their subsequent wind pattern, one way for the change is whether the TT mechanism is changed due to the increased anthropogenic gas concentrations. Figure 11 shows the lead-lag correlation of 1000–200 hPa mean TT and SST with DJF (0) Niño3.4 index during the periods of 1870–1919, 1950–1999 and 2049–2098 in MME. The patterns of ENSO-related TT anomalies are similar, with positive correlation coefficients developing and extending to the east, and the SST anomalies of remote region develop with TT anomalies. Interestingly, about one season after the mature phase of ENSO, the correlation coefficients in the period of 2049–2098 (Figure 11(i)–(l)) are about 0.1–0.2 higher than the period

of 1870–1919 (Figure 11(a)–(d)) over the TIO although ENSO activity does not change much (Figure 10(c) and (d)). Hu *et al.* (2013, personal communication) found that the strengthened Indian Ocean capacitor effect could be explained by the increased saturated specific humidity in global warming, which is also suitable for here. Response to the SST anomalies, through moist adiabatic adjustment in vertical, the upper tropospheric temperature anomalies could be written as $SST' + (L/C_p)RH(dq_s/dT) \cdot SST'$, where SST' is SST anomalies, L is latent heat of vaporization, C_p denotes the specific heat at constant pressure, RH is relative humidity and q_s is saturated specific humidity. According to the Clausius-Clapeyron equation, $dq_s/dT = q_s L / (R_v T^2) \sim 0.06 q_s$, R_v is the gas constant for water vapour. Under global warming, saturated specific humidity (q_s) increases. Since the relationship between TT anomalies and saturated specific humidity (q_s) is proportional, increased saturated specific humidity (q_s) leads to strengthened TT response. Therefore, on the condition of unchanged ENSO activity, the correlation coefficients are higher in the future. As a result, TT mechanism is strengthened in the future.

5.2.2. LHF related to TT mechanism

However, IOBM is partly caused by net heat flux (NHF). Although TT mechanism can explain the general temperature structure change, it does not directly relate to NHF changes. Moreover, NHF could be given by

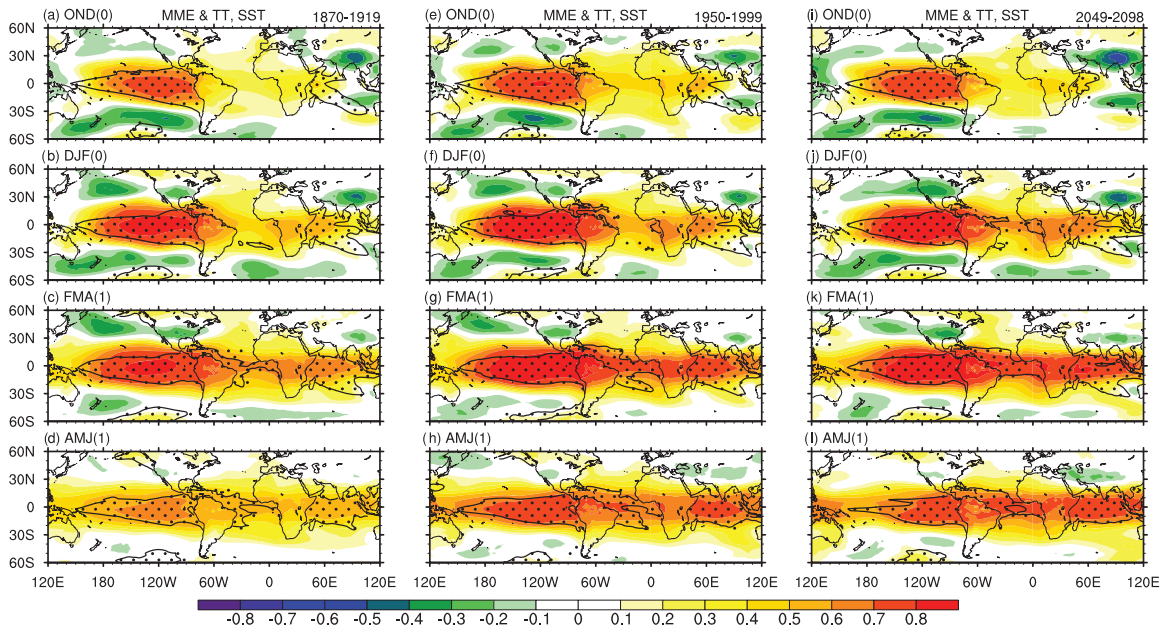


Figure 11. Multi-model ensemble correlation of 1000–200 hPa mean tropospheric temperature (TT; shaded) and SST (dotted) with DJF (0) Niño3.4 index during the periods of 1870–1919 (left panels, (a)–(e)), and 2049–2098 (right panels, (f)–(j)). The left strings above each panel indicate the months lead or lag DJF (0): OND (0) implies TT leads Niño3.4 index 2 months, DJF (0) implies TT and Niño3.4 index are simultaneous, FMA (1) implies TT lags Niño3.4 index 2 months, AMJ (1) implies TT lags Niño3.4 index 4 months. SST values exceeding 0.3 are dotted.

$Q_{NHF} = Q_L + Q_S + Q_{LW} + Q_{SW}$, where Q_L , Q_S , Q_{LW} and Q_{SW} are the LHF, SHF, LWR and SWR, respectively. Therefore, examining the NHF and its four components related to the remote SST warming provides a more precise way to investigate the TT mechanism or ‘atmospheric bridge’ mechanism. Figure 12 presents the correlation of NHF, LHF, SHF, LWR and SWR over the TIO with DJF (0) Niño3.4 index during the periods of 1870–1919, 1950–1999 and 2049–2098 for MME. IOBM mainly persists from boreal winter to summer, and the correlation coefficients are higher in 2049–2098 than in 1870–1919 (Figure 9). So the following study is mainly focused on the time period from November (0) to July (1). In Figure 12(a), the correlation coefficients of NHF during 2049–2098 are relatively smaller in the whole time from November (0) to July (1) than 1870–1919. Under global warming, more downward NHF or less upward NHF is conducive to the Indian Ocean warming. In the rest four figures (Figure 12(b)–(e)), the three components (SHF, LWR and SWR) do not show obvious change from November (0) to July (1) between 1870–1919 and 2049–2098. Only the correlation coefficients of LHF, which are similar to the NHF, are relatively small from November (0) to July (1) in the future. Especially, from November (0) to March (1), there are notable downward LHF over the TIO. Chiang and Lintner (2005) also suggested the importance of LHF in TT mechanism compared with the other three components. Comparing the periods of 1870–1919 and 2049–2098, more downward LHF causes more downward NHF, and less upward LHF causes less upward NHF. As a result, the LHF change makes a great contribution to the NHF change induced by TT mechanism in global warming.

Why the downward LHF over the TIO turns strong in global warming? Here is the possible reason from the perspective of qualitative analysis. The bulk formula for LHF can be expressed as

$$Q_L = \rho_a L C_E W (q_s(T) - RH q_s(T - \Delta T)) \quad (1)$$

where ρ_a is surface air density, L is the latent heat of evaporation, C_E is the transfer coefficient, W is the surface wind speed, RH is the relative humidity, T is SST, ΔT is sea minus air temperature difference and q_s is the saturated specific humidity following the Clausius-Clapeyron equation.

de Szoek *et al.* (2007) demonstrated that the term $q_s(T - \Delta T)$ can be decomposed:

$$\begin{aligned} q_s(T - \Delta T) &= q_s \left(T - \overline{\Delta T} - \Delta T' \right) \\ &= q_s \left(T - \overline{\Delta T} \right) + q'_s = \overline{q_s} + q'_s \end{aligned} \quad (2)$$

Then the term q'_s can be linearized about $T - \overline{\Delta T}$:

$$q'_s \cong -\Delta T' \left(\frac{\partial q_s}{\partial T} \right)_{T+\overline{\Delta T}} \quad (3)$$

where $\Delta T'$ is the anomaly of sea–air temperature difference. The vertical profile of air temperature anomalies is consistent with moist adiabatic vertical structure (Chiang and Sobel, 2002; Chiang and Lintner, 2005), and the air temperature anomalies increases with height. According to the vertical profile, the air temperature anomalies are higher than the SST anomalies and the anomaly of sea–air temperature difference is negative. Under global warming, the TT mechanism is strengthened, that is to say, the

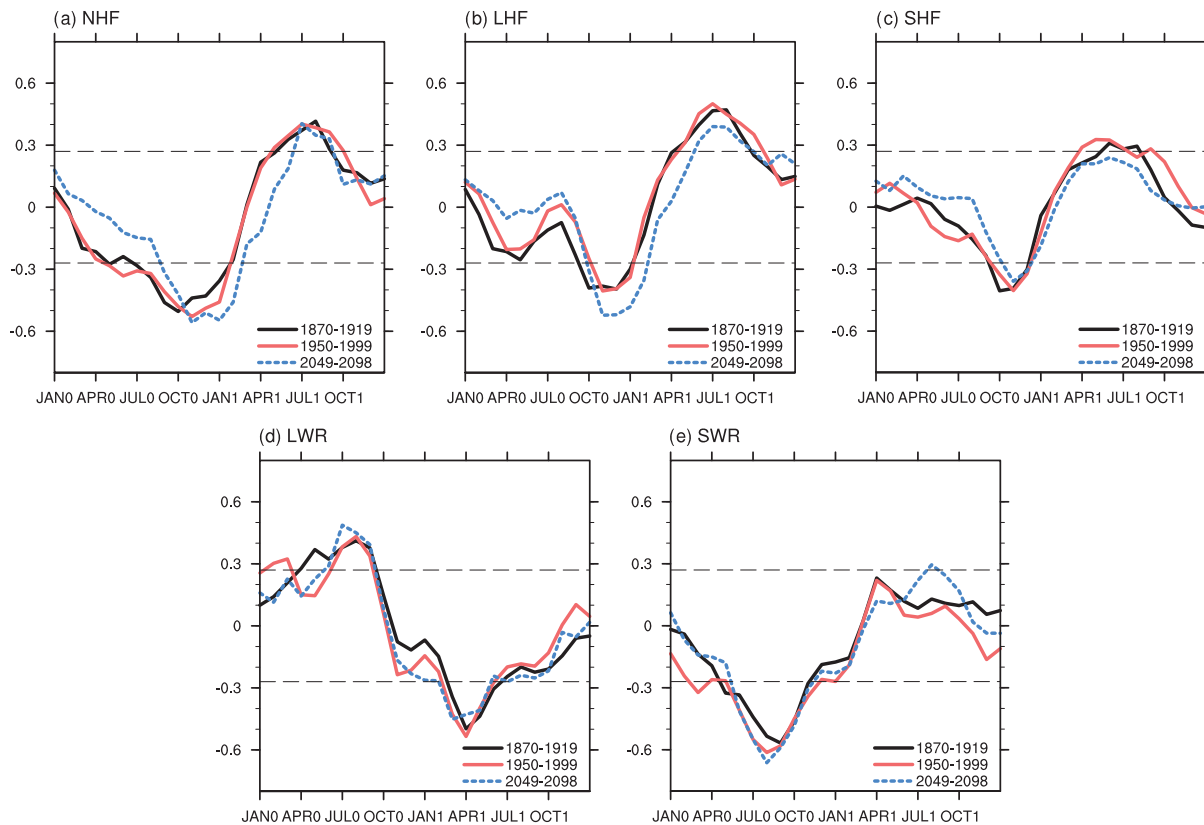


Figure 12. Multi-model ensemble correlation (upward positive) with DJF (0) Niño3.4 index for the periods of 1870–1919 (black solid line), 1950–1999 (red solid line) and 2049–2098 (blue dashed line): (a) NHF; (b) LHF; (c) SHF; (d) LWR; (e) SWR over the TIO. The horizontal dashed line indicates significant level reaches 95%.

correlation of TT anomalies with ENSO is strengthened (Figure 11). SST anomalies over the TIO before boreal winter do not change much, even decrease in global warming (Figure 11). Therefore, the enhanced ENSO-related TT anomalies decrease the negative sea–air temperature difference in the future. As a result, decreased anomalous sea–air temperature difference ($\Delta T'$) decreases upward or increases downward LHF by increasing q'_s according to the formula. It should be mentioned that the correlation coefficients of SHF and SWR show changes on similar magnitude compared with LHF since July (1) (Figure 12(c) and (e)). The SHF difference also should be associated with the sea–air temperature difference. The SWR might be a response to IOBM. The IOBM is stronger in the future, causing more cumulus clouds decrease the downward SWR. Above these are preliminary results of the qualitative analysis, the detailed processes are sophisticated and require further investigation.

5.3. The strengthened ENSO–IOBM relationship in the present

The SST anomalies over the TIO (Figure 8) and the correlation coefficients between ENSO and IOBM (Figure 9) are also strengthened in the period of 1950–1999. However, unlike the reasons in the future, the enhanced ENSO–IOBM relationship in the present is more likely caused by the shallower climatological thermocline

(Figure 10(a)). The shallower climatological thermocline strengthens the thermocline feedback and SST anomalies over the SWIO. Then the subsequent antisymmetric wind patterns are also stronger, further amplifying the NIO SST warming in the present. Xie *et al.* (2010) also emphasized the shallower thermocline is one of important factors for enhanced ENSO–IOBM relationship after 1970s.

It is noted that TT mechanism is also strengthened with unchanged ENSO activity in the present (Figure 11(e)–(h); Figure 10(c) and (d)), but the NHF and LHF do not change much from November (0) to July (1) compared with the past (Figure 12). Why does LHF related to TT mechanism remain unchanged in the present? The enhancement of SST anomalies induced by the shallower climatological thermocline can interpret this. Through TT anomalies are strengthened in the present, the SST anomalies over the TIO are also amplified. Thus, the anomalous sea–air temperature difference does not have a significant change, and LHF also change small. The situation in the present also demonstrates the importance of TT mechanism in the future, which makes the results of the previous qualitative analysis more robust.

6. Discussion and summary

On the basis of the historical scenario simulations and future climate projections of CMIP5 models, this study

have examined the ability of models to capture the ENSO–IOBM relationship, and investigated the characteristics of interdecadal change of ENSO–IOBM relationship as well as the response to the global warming.

Among 23 CMIP5 models, the capability of models in representing the IOBM depends largely on the simulation of ENSO in CMIP5 models, which also noted by Saji *et al.* (2006) who used the CMIP3 models. Moreover, some CMIP5 models can reproduce the unstable ENSO–IOBM relationship during 1870–2004 consistent with the observations (Huang *et al.*, 2010). Considering the simulation of ENSO, ENSO–IOBM relationship and interdecadal change, 6 of 23 CMIP5 models are chosen for further investigation.

ENSO has three different teleconnection processes to influence the IOBM, and the processes contribute to the interdecadal change of ENSO–IOBM relationship in 1970s in observation (Xie *et al.* 2010). On the basis of the six best CMIP5 models, the interdecadal change of ENSO–IOBM relationship is also associated with these three ENSO-related processes. During the HC period, the TT mechanism, oceanic Rossby waves and antisymmetric wind pattern are strong, prolonging the persistence of IOBM. However, during the LC period, the three processes are weak. Why are the three processes strengthened in the HC period? The results show that the shallow thermocline in the SWIO, increased interannual variability and prolonged periodicity of ENSO are all responsible for the interdecadal change in CMIP5 models, which is also demonstrated by the observation (Xie *et al.*, 2010).

The six best CMIP5 models can capture the interdecadal change between ENSO and IOBM, so they are useful to investigate the possible changes of ENSO–IOBM relationship in the future. Under global warming, the ENSO-related TIO warming is strengthened. However, the thermocline deepens in the SWIO, as a result of weakened Walker circulation in global warming (Held and Soden, 2006; Vecchi *et al.*, 2006; Tokinaga *et al.*, 2012). Furthermore, the interannual variability and periodicity of ENSO does not experience significant change in global warming, indicating unchanged ENSO activity. Accordingly, ENSO-related oceanic Rossby wave and antisymmetric wind pattern do not change much. Therefore, the deepened thermocline and unchanged ENSO activity are not the possible reasons for the enhancement of TIO warming.

Excluding the influence of ocean processes and their subsequent wind pattern, the ENSO-related TIO warming is strengthened by the enhanced TT mechanism. And strengthened TT response is possibly due to the increased mean moisture content in global warming (Held and Soden, 2006). Under global warming, higher temperature increases saturated specific humidity in the air. Since the relationship between TT anomalies and saturated specific humidity is proportional, increased saturated specific humidity leads to strengthened TT response. As a result, despite the unchanged ENSO activity, the TT mechanism is strengthened in the future.

Though the TT mechanism can explain the general temperature structure change, it does not directly relate to

NHF changes. In this study, the NHF and its four components related to the remote SST warming are examined. The results reveal that there is more downward NHF over the TIO, which is conducive to the TIO warming, and the LHF change makes a great contribution to the NHF change in global warming. The weakened upward or strengthened downward LHF is possibly due to the decreased anomalous sea–air temperature difference by strengthened TT mechanism.

In the present, through TT mechanism is strengthened, the SST anomalies over the TIO are also amplified due to the shallower climatological thermocline in the SWIO. Therefore, the anomalous sea–air temperature difference does not have a significant change, and LHF also change small. Unlike the reasons in the future, the enhanced ENSO–IOBM relationship in the present is more likely caused by the shallower climatological thermocline.

The conclusion that the ENSO-related TIO SST anomalies are strengthened under global warming is convincing, which is consistent with Zheng *et al.* (2011). While we interpret the enhanced ENSO–IOBM relationship by TT mechanism in this study, the TT mechanism and it contained various processes are very complicated. TT mechanism is only one of the pathways that ENSO influences the Indian Ocean. The challenge for the response of IOBM to ENSO in global warming is to understand what changes of detailed processes in the TT mechanism are, determine which pathway is most important in strengthened ENSO–IOBM relationship, and how each pathway changes in global warming.

Acknowledgements

We acknowledge the World Climate Research Program's Working Group on Coupled Modeling, which is responsible for CMIP, and we thank the climate modeling groups (listed in Table 1 of this article) for producing and making available their model output. For CMIP the U.S. Department of Energy's Program for Climate Model Diagnosis and Intercomparison provides coordinating support and led development of software infrastructure in partnership with the Global Organization for Earth System Science Portals. This work was supported by the National Basic Research Program of China (2012CB955604 and 2011CB309704), the Strategic Priority Research Program of the Chinese Academy of Sciences (XDA05090402), and the National Natural Science Foundation of China (41275083 and 91337105). The authors thank Prof. Wu Renguang and two anonymous reviewers as well as editors for their useful comments.

References

- Alexander MA, Blade I, Newman M, Lanzante JR, Lau NC, Scott JD. 2002. The atmospheric bridge: the influence of ENSO teleconnections on air–sea interaction over the global oceans. *J. Clim.* **15**(16): 2205–2231, DOI: 10.1175/1520-0442(2002)015<2205:tabtio>2.0.co;2.
- Bellenger H, Guilyardi E, Leloup J, Lengaigne M, Vialard J. 2013. ENSO representation in climate models: from CMIP3 to CMIP5. *Clim. Dyn.*, DOI: 10.1007/s00382-013-1783-z.

- Chakravorty S, Chowdary JS, Gnanaseelan C. 2013. Epochal changes in the seasonal evolution of tropical Indian Ocean warming associated with El Niño. *Clim. Dyn.* **1–18**, DOI: 10.1007/s00382-013-1666-3.
- Charney JG. 1963. A note on large-scale motions in the tropics. *J. Atmos. Sci.* **20**(6): 607–609, DOI: 10.1175/1520-0469(1963)020<0607:anolsm>2.0.co;2.
- Chiang JCH, Lintner BR. 2005. Mechanisms of remote tropical surface warming during El Niño. *J. Clim.* **18**(20): 4130–4149, DOI: 10.1175/jcli3529.1.
- Chiang JCH, Sobel AH. 2002. Tropical tropospheric temperature variations caused by ENSO and their influence on the remote tropical climate. *J. Clim.* **15**(18): 2616–2631, DOI: 10.1175/1520-0442(2002)015<2616:tvtvcb>2.0.co;2.
- Chowdary JS, Gnanaseelan C. 2007. Basin-wide warming of the Indian Ocean during El Niño and Indian Ocean dipole years. *Int. J. Climatol.* **27**(11): 1421–1438, DOI: 10.1002/joc.1482.
- Chowdary JS, Gnanaseelan C, Xie SP. 2009. Westward propagation of barrier layer formation in the 2006–07 Rossby wave event over the tropical southwest Indian Ocean. *Geophys. Res. Lett.* **36**, DOI: 10.1029/2008gl036642.
- Chowdary JS, Xie SP, Tokinaga H, Okumura YM, Kubota H, Johnson N, Zheng XT. 2012. Interdecadal variations in ENSO teleconnection to the Indo-Western Pacific for 1870–2007. *J. Clim.* **25**(5): 1722–1744, DOI: 10.1175/jcli-d-11-00070.1.
- Chowdary JS, Parekh A, Gnanaseelan C, Sreenivas P. 2014. Inter-decadal modulation of ENSO teleconnections to the Indian Ocean in a coupled model: special emphasis on decay phase of El Niño. *Global Planet. Change* **112**: 33–40, DOI: 10.1016/j.gloplacha.2013.11.003.
- Chu J-E, Ha K-J, Lee J-Y, Wang B, Kim B-H, Chung C. 2013. Future change of the Indian Ocean basin-wide and dipole modes in the CMIP5. *Clim. Dyn.* **1–17**, DOI: 10.1007/s00382-013-2002-7.
- Collins M, An SI, Cai WJ, Ganachaud A, Gouliardi E, Jin FF, Jochum M, Lengaigne M, Power S, Timmermann A, Vecchi G, Wittenberg A. 2010. The impact of global warming on the tropical Pacific ocean and El Niño. *Nat. Geosci.* **3**(6): 391–397, DOI: 10.1038/ngeo868.
- De Szoek SP, Xie SP, Miyama T, Richards KJ, Small RJO. 2007. What maintains the SST front north of the eastern Pacific equatorial cold tongue? *J. Clim.* **20**(11): 2500–2514, DOI: 10.1175/jcli4173.1.
- Du Y, Xie SP, Huang G, Hu K. 2009. Role of air-sea interaction in the long persistence of El Niño-Induced North Indian Ocean warming. *J. Clim.* **22**(8): 2023–2038.
- Du Y, Yang L, Xie SP. 2011. Tropical Indian Ocean influence on Northwest Pacific tropical cyclones in summer following strong El Niño. *J. Clim.* **24**(1): 315–322, DOI: 10.1175/2010jcli3890.1.
- Du Y, Xie S-P, Yang Y-L, Zheng X-T, Liu L, Huang G. 2013. Indian Ocean variability in the CMIP5 multimodel ensemble: the basin mode. *J. Clim.* **26**(18): 7240–7266, DOI: 10.1175/jcli-d-12-00678.1.
- Gill AE. 1980. Some simple solutions for heat-induced tropical circulation. *Q. J. R. Meteorol. Soc.* **106**(449): 447–462, DOI: 10.1256/smsqj.44904.
- Gong H, Wang L, Chen W, Wu R, Wei K, Cui X. 2013. The climatology and interannual variability of the East Asian winter monsoon in CMIP5 models. *J. Clim.*, DOI: 10.1175/jcli-d-13-00039.1.
- Held IM, Soden BJ. 2006. Robust responses of the hydrological cycle to global warming. *J. Clim.* **19**(21): 5686–5699, DOI: 10.1175/jcli3990.1.
- Horel JD, Wallace JM. 1981. Planetary-scale atmospheric phenomena associated with the southern oscillation. *Mon. Weather Rev.* **109**(4): 813–829, DOI: 10.1175/1520-0493(1981)109<0813:psapaw>2.0.co;2.
- Hu K, Huang G, Huang R. 2011. The impact of tropical Indian Ocean variability on summer surface air temperature in China. *J. Clim.* **24**(20): 5365–5377.
- Hu K, Huang G, Qu X, Huang R. 2012a. The impact of Indian Ocean variability on high temperature extremes across the southern Yangtze River valley in late summer. *Adv. Atmos. Sci.* **29**(1): 91–100.
- Hu K, Huang G, Wu R. 2012b. A strengthened influence of ENSO on august high temperature extremes over the southern Yangtze River Valley since the late 1980s. *J. Clim.* **26**(7): 2221–2205, DOI: 10.1175/jcli-d-12-00277.1.
- Huang BH, Kinter JL. 2002. Interannual variability in the tropical Indian Ocean. *J. Geophys. Res. Oceans* **107**(C11), DOI: 10.1029/2001jc001278.
- Huang G, Hu KM, Xie SP. 2010. Strengthening of Tropical Indian Ocean teleconnection to the Northwest Pacific since the mid-1970s: an atmospheric GCM study. *J. Clim.* **23**(19): 5294–5304, DOI: 10.1175/2010jcli3577.1.
- Huang G, Qu X, Hu KM. 2011. The impact of the Tropical Indian Ocean on South Asian high in boreal summer. *Adv. Atmos. Sci.* **28**(2): 421–432, DOI: 10.1007/s00376-010-9224-y.
- Kawamura R, Matsuura T, Iizuka S. 2001. Role of equatorially asymmetric sea surface temperature anomalies in the Indian Ocean in the Asian summer monsoon and El Niño-Southern Oscillation coupling. *J. Geophys. Res. Atmos.* **106**(D5): 4681–4693, DOI: 10.1029/2000jd900610.
- Kim ST, Yu JY. 2012. The two types of ENSO in CMIP5 models. *Geophys. Res. Lett.* **39**, DOI: 10.1029/2012gl052006.
- Klein SA, Soden BJ, Lau N-C. 1999. Remote sea surface temperature variations during ENSO: evidence for a tropical atmospheric bridge. *J. Clim.* **12**(4): 917–932, DOI: 10.1175/1520-0442(1999)012<0917:rsstvd>2.0.co;2.
- Krishnamurthy V, Kirtman BP. 2003. Variability of the Indian Ocean: relation to monsoon and ENSO. *Q. J. R. Meteorol. Soc.* **129**(590): 1623–1646, DOI: 10.1256/qj.02.166.
- Lau NC. 1997. Interactions between global SST anomalies and the midlatitude atmospheric circulation. *Bull. Am. Meteorol. Soc.* **78**(1): 21–33, DOI: 10.1175/1520-0477(1997)078<0021:ibgsaa>2.0.co;2.
- Lau NC, Nath MJ. 1996. The role of the "atmospheric bridge" in linking tropical Pacific ENSO events to extratropical SST anomalies. *J. Clim.* **9**: 2036–2057.
- Lau NC, Nath MJ. 2000. Impact of ENSO on the variability of the Asian-Australian monsoons as simulated in GCM experiments. *J. Clim.* **13**(24): 4287–4309, DOI: 10.1175/1520-0442(2000)013<4287:ioeotv>2.0.co;2.
- Lau NC, Nath MJ. 2003. Atmosphere–ocean variations in the Indo-Pacific sector during ENSO episodes. *J. Clim.* **16**(1): 3–20, DOI: 10.1175/1520-0442(2003)016<0003:aoviti>2.0.co;2.
- Masumoto Y, Meyers G. 1998. Forced Rossby waves in the southern tropical Indian Ocean. *J. Geophys. Res. Oceans* **103**(C12): 27589–27602, DOI: 10.1029/98jc02546.
- Matsuno T. 1966. Quasi-geostrophic motions in the equatorial area. *J. Meteor. Soc. Jpn.* **44**(1): 25–43.
- Murtugudde R, Busalacchi AJ. 1999. Interannual variability of the dynamics and thermodynamics of the tropical Indian Ocean. *J. Clim.* **12**(8): 2300–2326, DOI: 10.1175/1520-0442(1999)012<2300:ivotda>2.0.co;2.
- Pan YH, Oort AH. 1983. Global climate variations connected with sea-surface temperature anomalies in the eastern equatorial Pacific-Ocean for the 1958–73 period. *Mon. Weather Rev.* **111**(6): 1244–1258, DOI: 10.1175/1520-0493(1983)111<1244:gcvvcs>2.0.co;2.
- Park HS, Chiang JCH, Lintner BR, Zhang GJ. 2010. The delayed effect of major El Niño events on Indian monsoon rainfall. *J. Clim.* **23**(4): 932–946, DOI: 10.1175/2009jcli2916.1.
- Qu X, Huang G. 2012a. An enhanced influence of tropical Indian Ocean on the South Asia High after the late 1970s. *J. Clim.* **25**(20): 6930–6941, DOI: 10.1175/jcli-d-11-00696.1.
- Qu X, Huang G. 2012b. Impacts of tropical Indian Ocean SST on the meridional displacement of East Asian jet in boreal summer. *Int. J. Climatol.* **32**(13): 2073–2080, DOI: 10.1002/joc.2378.
- Rayner NA, Parker DE, Horton EB, Folland CK, Alexander LV, Rowell DP, Kent EC, Kaplan A. 2003. Global analyses of sea surface temperature, sea ice, and night marine air temperature since the late nineteenth century. *J. Geophys. Res. Atmos.* **108**(D14): 4407, DOI: 10.1029/2002jd002670.
- Saji NH, Xie SP, Yamagata T. 2006. Tropical Indian Ocean variability in the IPCC twentieth-century climate simulations. *J. Clim.* **19**(17): 4397–4417, DOI: 10.1175/jcli3847.1.
- Schott FA, Xie SP, McCreary JP. 2009. Indian Ocean circulation and climate variability. *Rev. Geophys.* **47**: RG1002, DOI: 10.1029/2007rg000245.
- Sobel AH, Bretherton CS. 2000. Modeling tropical precipitation in a single column. *J. Clim.* **13**(24): 4378–4392, DOI: 10.1175/1520-0442(2000)013<4378:mtpias>2.0.co;2.
- Soden BJ. 2000. The sensitivity of the tropical hydrological cycle to ENSO. *J. Clim.* **13**(3): 538–549, DOI: 10.1175/1520-0442(2000)013<0538:tsotth>2.0.co;2.
- Su H, Neelin JD, Meyerson JE. 2003. Sensitivity of tropical tropospheric temperature to sea surface temperature forcing. *J. Clim.* **16**(9): 1283–1301, DOI: 10.1175/1520-0442-16.9.1283.
- Tao W, Huang G, Hu K, Qu X, Wen G, Gong Y. 2013. Different influences of two types of El Niños on the Indian Ocean SST variations. *Theor. Appl. Climatol.* **1–10**, DOI: 10.1007/s00704-013-1022-x.
- Thomson AM, Calvin KV, Smith SJ, Kyle GP, Volke A, Patel P, Delgado-Arias S, Bond-Lamberty B, Wise MA, Clarke LE,

- Edmonds JA. 2011. RCP4.5: a pathway for stabilization of radiative forcing by 2100. *Clim. Change* **109**(1–2): 77–94, DOI: 10.1007/s10584-011-0151-4.
- Tokinaga H, Xie S-P, Deser C, Kosaka Y, Okumura YM. 2012. Slowdown of the Walker circulation driven by tropical Indo-Pacific warming. *Nature* **491**(7424): 439–443.
- Vecchi GA, Soden BJ, Wittenberg AT, Held IM, Leetmaa A, Harrison MJ. 2006. Weakening of tropical Pacific atmospheric circulation due to anthropogenic forcing. *Nature* **441**(7089): 73–76, DOI: 10.1038/nature04744.
- Venzke S, Latif M, Villwock A. 2000. The coupled GCM ECHO-2. Part II: Indian Ocean response to ENSO. *J. Clim.* **13**(8): 1371–1383, DOI: 10.1175/1520-0442(2000)013<1371:tcge>2.0.co;2.
- Wallace JM. 1992. Effect of deep convection on the regulation of tropical sea-surface temperature. *Nature* **357**(6375): 230–231, DOI: 10.1038/357230a0.
- Wang B, Yang J, Zhou TJ. 2008. Interdecadal changes in the major modes of Asian-Australian monsoon variability: strengthening relationship with ENSO since the late 1970s. *J. Clim.* **21**(8): 1771–1789, DOI: 10.1175/2007jcli1981.1.
- Wu R, Yeh S-W. 2010. A further study of the tropical Indian Ocean asymmetric mode in boreal spring. *J. Geophys. Res. Atmos.* **115**(D8): D08101, DOI: 10.1029/2009jd012999.
- Wu R, Kirtman BP, Krishnamurthy V. 2008. An asymmetric mode of tropical Indian Ocean rainfall variability in boreal spring. *J. Geophys. Res. Atmos.* **113**(D5), DOI: 10.1029/2007jd009316.
- Xie SP, Philander SGH. 1994. A coupled ocean–atmosphere model of relevance to the itcz in the eastern Pacific. *Tellus A Dyn. Meteorol. Oceanogr.* **46**(4): 340–350, DOI: 10.1034/j.1600-0870.1994.t01-1-00001.x.
- Xie SP, Annamalai H, Schott FA, McCreary JP Jr. 2002. Structure and mechanisms of south Indian Ocean climate variability. *J. Clim.* **15**(8): 864–878.
- Xie SP, Hu K, Hafner J, Tokinaga H, Du Y, Huang G, Sampe T. 2009. Indian Ocean capacitor effect on Indo-western Pacific climate during the summer following El Niño. *J. Clim.* **22**(3): 730–747.
- Xie SP, Du Y, Huang G, Zheng XT, Tokinaga H, Hu KM, Liu QY. 2010. Decadal shift in El Niño influences on Indo-Western Pacific and East Asian climate in the 1970s. *J. Clim.* **23**(12): 3352–3368, DOI: 10.1175/2010jcli3429.1.
- Yu LS, Rienecker MM. 1999. Mechanisms for the Indian Ocean warming during the 1997–98 El Niño. *Geophys. Res. Lett.* **26**(6): 735–738, DOI: 10.1029/1999gl900072.
- Yulaeva E, Wallace JM. 1994. Signature of ENSO in global temperature and precipitation fields derived from the microwave sounding unit. *J. Clim.* **7**(11): 1719–1736, DOI: 10.1175/1520-0442(1994)007<1719:tsoeig>2.0.co;2.
- Zheng XT, Xie SP, Liu QY. 2011. Response of the Indian Ocean basin mode and its capacitor effect to global warming. *J. Clim.* **24**(23): 6146–6164, DOI: 10.1175/2011jcli4169.1.
- Zheng X-T, Xie S-P, Du Y, Liu L, Huang G, Liu Q. 2013. Indian Ocean dipole response to global warming in the CMIP5 multimodel ensemble. *J. Clim.* **26**(16): 6067–6080, DOI: 10.1175/jcli-d-12-00638.1.